Title

Numerical simulation of rainfall-induced deformations of embankments considering the coupled hydro-mechanical behavior of unsaturated soils

Authors

Zheng, Yewei
Wu, Hao
Luan, Xiaohan
et al.

Publication Date

2024-11-01

DOI

10.1016/j.compgeo.2024.106714

Peer reviewed

Numerical Simulation of Rainfall-Induced Deformations of Embankments Considering the Coupled Hydro-Mechanical Behavior of Unsaturated Soils

Yewei Zheng[1,*], Hao Wu[2], Xiaohan Luan[3], and John S. McCartney[4]

*[1] Professor, School of Civil Engineering, Wuhan University, Wuhan, Hubei 430072, China; Email: yzheng@whu.edu.cn (*corresponding author); ORCID Number: 0000-0001-9038-4113*

[2] formerly Master Student, School of Civil Engineering, Wuhan University, Wuhan, Hubei 430072, China; Email: ahwuhao@whu.edu.cn;

[3] Ph.D. Student, School of Civil Engineering, Wuhan University, Wuhan, Hubei 430072, China; Email: xhluan@whu.edu.cn;

[4] Professor, Department of Structural Engineering, University of California, San Diego, La Jolla, CA 92093-0085 USA; Email: mccartney@ucsd.edu; ORCID: 0000-0001-7279-3490;

Abstract: This paper presents numerical simulations of the deformation response of unsaturated embankments subjected to rainfall infiltration using a coupled hydro-mechanical constitutive model for unsaturated soils. The constitutive model accounts for the influence of degree of saturation on the stress-strain behavior and the influence of void ratio on the water retention behavior. The constitutive model was implemented in the finite difference program FLAC, calibrated using triaxial test data, and validated using measurements of wetting-induced deformations of embankment models from centrifuge tests. The validation demonstrates that the constitutive model can capture the coupled hydro-mechanical behavior of unsaturated soils under wetting conditions. Simulations of the hydro-mechanical response of unsaturated embankments subjected to rainfall infiltration indicate that the differential settlement across the top surface of the embankment between the centerline and shoulder increases significantly during rainfall infiltration, which could result in severe damage to overlying transportation infrastructure. As the cumulative infiltration increases, shear strains accumulate and form a potential failure surface at a shallow depth of approximately 2 m from the slope surface. Insights into the hydro-mechanical response of unsaturated embankments subjected to rainfall infiltration gained from the model will be useful for considering climate change effects in design and construction of compacted embankments.

Keywords: Unsaturated soil; Hydro-mechanical behavior; Embankment; Rainfall infiltration; Rainfall-induced deformation

1 Introduction

The compacted fill in embankments is typically designed with appropriate drainage to remain in unsaturated conditions, but temporal changes in the degree of saturation are expected due to transient interaction with the environment. In particular, sustained rainfall infiltration will result in in suction reduction in unsaturated fills, which could lead to deformations and instability of embankments under self-weight loading (Lim et al., 1996; Sassa et al., 2009; Abbate et al., 2021). This is particularly the case for embankment fills that are compacted dry of optimum (Mitchell et al. 1965). Most studies on environmental interaction with embankments focused on rainfall-induced instability issues in embankment slopes without consideration of the deformation response (e.g., Moriwaki et al., 2004, Wang et al., 2010, Zhang et al. 2011). For example, Zhang et al. (2011) found that the unsaturated embankment slopes experienced shallow slip failures during rainfall in centrifuge modeling tests. However, rainfall-induced deformations of embankments are also important to consider even when failure does not occur, as deformations could lead to distress of overlying transportation infrastructure and corresponding reduction in service performance, corresponding to significant economic costs for maintenance and repair. Wang et al. (2021) conducted a series of centrifuge tests to investigate the impacts of rainfall intensity and initial soil conditions (e.g. void ratio and degree of saturation) on the rainfall-induced deformations of embankment slopes, as well as the failure pattern. However, the evolution of suction and the corresponding development of deformations within the embankments under rainfall infiltration were not studied in detail, emphasizing the need to further evaluate this problem with more advanced constitutive models.

It is well known that unsaturated soils experience changes in the degree of saturation and suction upon wetting, which could lead to changes in volume and shear strength, and possibly water retention behavior (Zhou et al., 2012a, 2012b). Earlier studies on unsaturated soils consider the stress-strain behavior and water retention behavior separately using independent mechanical and hydraulic models, respectively (Cui and Delage, 1996; Gens, 1996; Georgiadis et al., 2005). However, many recent experimental studies reveal the mechanical and hydraulic behavior of unsaturated soils are interconnected (Sharma, 1998; Wheeler and Sivakumar, 2000; Jotisankasa et al., 2007; Sun et al., 2010; McCartney and Behbehani 2021). It is well known that the hydraulic parameters (e.g., suction, or saturation) affect the shear strength (Lee et al., 2005; Sun et al., 2000; Thu et al., 2007; Toll, 1990; Delage and Graham, 1996; Sivakumar and Wheeler, 2000) and stiffness (e.g., Khosravi and McCartney 2012) of unsaturated soils. Further, it is well known than the soil-water retention curve (SWRC) is affected by soil deformations during compression or shearing (Adams, 1996; Gallipoli et al., 2003; Miller et al., 2008; Sharma, 1998; Sun et al., 2007; Vanapalli et al., 1999; Zakaria, 1994). For example, Sun et al. (2007) found that isotropic loading and unloading of compacted Pearl clay under constant suction resulted in changes of the degree of saturation, and that wetting under constant mean net stress leaded to decreases in volume. For the constitutive model proposed by Zhou and Sheng (2015), a sub-loading surface and a unified hardening parameter are introduced to interpret the effect of initial density on the coupled hydro-mechanical behavior of compacted soils, and two hydro-mechanical interaction parameters are introduced to quantify the effect of saturation on the compressibility and the effect of volume change on the variation in saturation. Advanced constitutive models that can capture the coupled hydro-mechanical behavior of unsaturated soils are necessary to estimate the deformation response of unsaturated soils.

Alonso et al. (1990) proposed an elastoplastic constitutive model for unsaturated soils, referred to as the Barcelona Basic Model (BBM), using the net stress and suction as two independent stress state variables. Following the BBM framework, a series of constitutive models for unsaturated soils have been developed (Wheeler and Sivakumar, 1995; Chui and Ng, 2003; Sheng et al.,2008; Gens, 2009). However, these models did not consider the coupled hydro-mechanical behavior of unsaturated soils and could not capture the transition between the unsaturated and saturated states. Wheeler (1996) was among the first to acknowledge this interaction between the mechanical and hydraulic behavior. Since then, many constitutive models have been proposed to incorporate the coupled hydro-mechanical behavior of unsaturated soils by integrating the suction and degree of saturation into the effective stress and considering the volume change behavior on the water retention behavior (Kato et al., 1996; Karube et al., 1997; Khalili et al., 2008; Gallipoli et al., 2003; Sun et al., 2007; Sun and Sun, 2012; Wheeler et al., 2003; Xiong et al., 2019; Zhang and Ikariya, 2011; Zhou et al. 2012a, 2012b). These constitutive models can better capture the deformation response of unsaturated soils and are suitable for investigating engineering problems.

Due to the complex form of the constitutive models for unsaturated soils, only a few models have been implemented into computer programs to investigate boundary value problems. The implementation of the BBM in CODE_BRIGHT (Olivella et al. 1996) has been used to study many engineering problems. For example, Alonso et al. (2005) utilized the BBM in CODE_BRIGHT to simulate the deformation response of a zoned earth dam throughout the construction, impoundment, and rainfall stages. Jamei et al. (2015) studied the rainfall-induced local and shallow failures of unsaturated slopes using CODE_BRIGHT. Rutqvist et al. (2011) implemented a thermo-elasto-plastic version of the BBM into the TOUGH-FLAC simulator to analyze the behavior of unsaturated soils in nuclear waste repositories. Zheng et al. (2017) implemented the BBM in into FLAC and investigated the wetting-induced deformations of unsaturated embankments due water table rise. In most computer programs, the numerical simulations involving BBM did not consider the hydro-mechanical coupling in unsaturated soils. Hence, there is a need to implement more advanced constitutive models into computer program to accurately capture the coupled hydro-mechanical behavior of unsaturated soils, which can be used to investigate boundary value problems related to the rainfall-induced deformation response of embankments.

In this study, a coupled hydro-mechanical constitutive model for unsaturated soils is introduced, which accounts for the influence of degree of saturation on the stress-strain behavior and the influence of void ratio on the water retention behavior. The constitutive model is implemented in the two-dimensional finite difference program FLAC and calibrated using constant water content triaxial test data. The constitutive model for unsaturated soil is then used to simulate the hydro-mechanical response of unsaturated embankments subjected to rainfall infiltration to provide insights into the design and construction of compacted embankments under climate change conditions.

2 A coupled hydro-mechanical constitutive model

The coupled hydro-mechanical constitutive model of unsaturated soils in this study is developed based on the elasto-plastic framework incorporating the water retention behavior proposed by Sun et al. (2007). The mechanical part is consistent with that of Sun et al. (2007), while the hydraulic part is novel. The SWRC adopts the van Genuchten (1980) model but considers the influence of void ratio on the SWRC. As this study focuses on the wetting-induced deformations of unsaturated soils under rainfall infiltration, hydraulic hysteresis is not considered.

2.1 Stress-strain behavior

The effective stress σ'_{ij} is defined as

$$\sigma_{ij}^{'} = \sigma_{ij} - u_a\delta_{ij} + S_r s\delta_{ij} \tag{1}$$

where σ_{ij} is the total stress, u_a is the pore air pressure, s is the suction, S_r is the degree of saturation, and δ_{ij} is the Kronecker delta. In Eq. (1), σ'_{ij} is equal to Bishop's effective stress with the weighting factor χ equal to S_r. For the soils evaluated in this study, the residual saturation is equal to zero, so S_r is equal to the effective saturation S_e, which permits the SWRC to be directly integrated into the effective stress (Lu et al. 2010). When S_r is equal to 1, the effective stress σ'_{ij} transitions into Terzaghi's effective stress for saturated conditions. The mean effective stress p' is expressed as follows:

$$p' = p - u_a + S_r s \tag{2}$$

where p is the mean total stress.

The expression for the load collapse (LC) yield curve, which describes the relationship between the mean effective yield stress p'_y for unsaturated conditions at suction s and the yield stress p'_{0y} for saturated condition in the p'-s plane in the isotropic stress state, is as follows:

$$p_y' = p_n^{'}\left(\frac{p_{0y}'}{p_y'}\right)^{\frac{\lambda(0)-\kappa}{\lambda(s)-\kappa}} \tag{3}$$

Where p'_y = mean effective stress for the soil at suction s; p'_n = mean effective stress where no deformation occurs when suction decreases during wetting, which is also the mean effective stress corresponding to the intersection of compression curves having different suction values at high values of mean effective stress; p'_{0y} = mean effective yield stress for the soil in saturated conditions; $\lambda(0)$ = slope of normal consolidation line (NCL) for saturated condition; $\lambda(s)$ = slope of NCL at suction s; κ = swelling index. Following the approach of Sun et al. (2007), $\lambda(s)$ is expressed as:

$$\lambda(s) = \lambda(0) + \frac{\lambda_s\ s}{p_{at} + s} \tag{4}$$

where p_{at} = atmospheric pressure; and λ_s = material parameter that controls changes in the slope of the NCL with changes in suction. Eq. (4) is different from the BBM in that the NCLs for unsaturated soils with different suction values converge with the NCL for saturated soils as the mean effective stress increases, which is observed in experimental studies on compression to high stresses (Mun and McCartney 2017). The LC yield curves under isotropic conditions are shown in Fig. 1. The LC curves expand due to change in suction, resulting in plastic volumetric strains. In the current version of the coupled hydro-mechanical model, the suction-increase (SI) yield curve is not included, as this study focuses on the deformation behavior of unsaturated soils under the wetting process, in which the initial suction is the maximum suction experienced in the past.

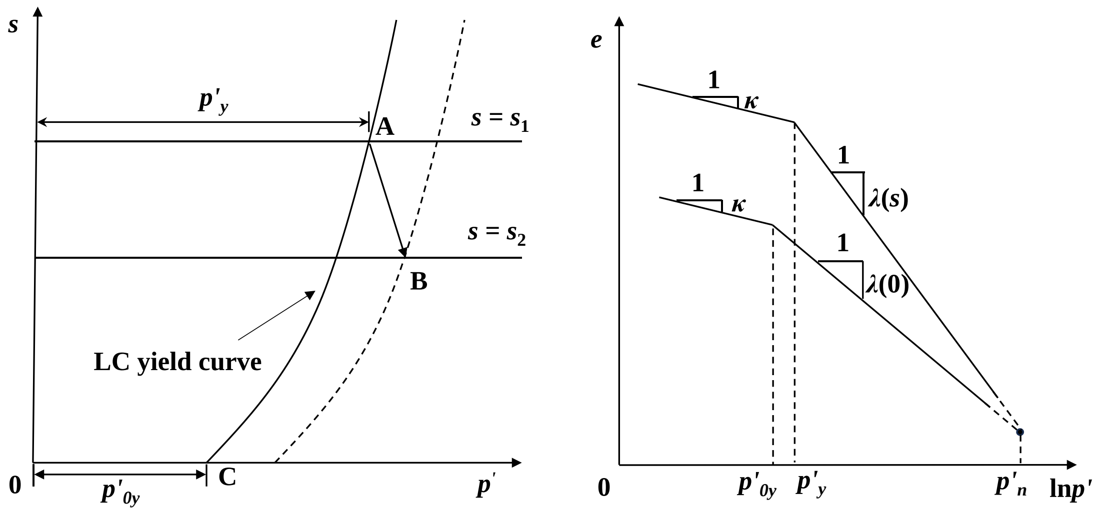

Fig.1 Effective stress-based LC yield curves under isotropic conditions.

The yield function in p'-q space is defined according to the modified Cam-clay model and assumes an associated flow rule for the convenience of model implementation in FLAC. This assumption is also suitable for unsaturated fills with a higher fines content that may not have significant dilation during shearing. Specifically, the yield function f and potential function g are represented by Eq. (5):

$$f = g = q^2 + M^2 p'\left(p' - p'_y\right) = 0 \tag{5}$$

where M = slope of the critical state line; q = deviator stress. The yield curves in the p'-q plane and the yield surface in p'-q-s space are shown in Fig. 2(a) and 2(b), respectively.

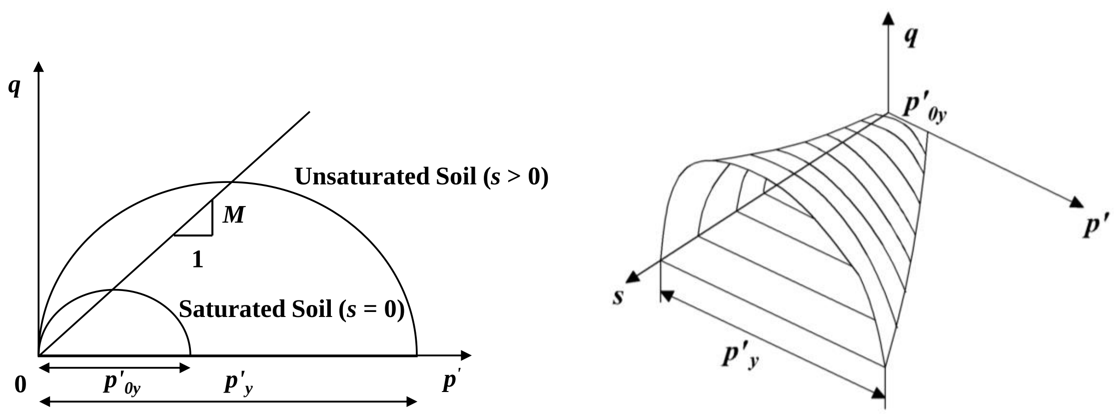

(a) (b)

Fig. 2 Yield surface: (a) p'-q plane for different suctions; (b) p'-q-s space.

When the stress state is inside the LC yield curve, elastic volumetric strain increments are calculated as follows:

$$d\varepsilon_v^e = \frac{\kappa dp'}{(1+e)p'} \tag{6}$$

where e is the current void ratio. When the stress state is on the LC yield curve, plastic volumetric strain increments are calculated as follows:

$$d\varepsilon_v^p = \frac{(\lambda(0)-\kappa)dp_{0y}^{'}}{(1+e)p_{0y}'} \tag{7}$$

The total volumetric strain is the sum of the elastic and plastic volumetric strains:

$$d\varepsilon_v = d\varepsilon_v^e + d\varepsilon_v^p \tag{8}$$

The specific volume v is then updated with the increments in total volumetric strain:

$$v^{new} = v^{old}(1 - d\varepsilon_v) \tag{9}$$

2.2 Water retention behavior

The van Genuchten (1980) SWRC model is used to describe the relationship between the degree of saturation S_r and the suction s. Assuming that the residual degree of saturation $S_r^w = 0$, S_r is equal to the effective saturation S_e, and the SWRC takes the following form:

$$S_r = S_e = \left(\frac{1}{1+(\alpha s)^n}\right)^m \tag{10}$$

where α, m, and n are fitting parameters with m = 1-1/n.

Previous studies on boundary value problems involving unsaturated soils typically assume a single SWRC. In this study, to simulate the coupled hydro-mechanical behavior of unsaturated soils more accurately, the relationship between the void ratio e and the air entry value $1/\alpha$ is introduced into the van Genuchten (1980) SWRC model to incorporate the influence of volume change on the water retention behavior of unsaturated soils. This study adopted the linear relationship between e and $1/\alpha$ proposed by Nuth and Laloui (2008), as follows:

$$1/\alpha = -Ae + B \tag{11}$$

where A and B are fitting parameters, which can be determined by fitting the soil-water retention curve to data for soils compacted to different void ratios. An example of how the SWRCs will change as the void ratio decreases is depicted in Fig 3.

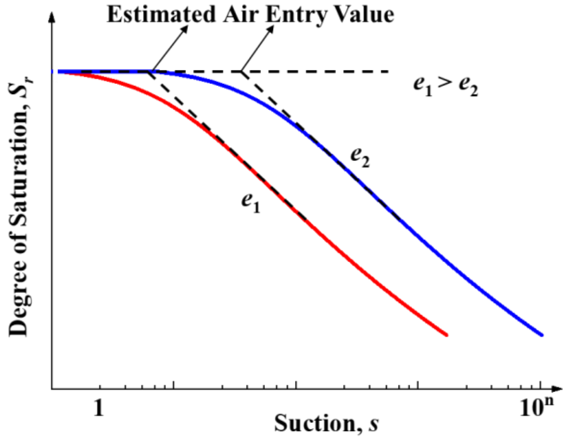

Fig. 3 Soil water retention curves for different void ratios.

3 Model implementation and calibration

3.1 Model implementation

The coupled hydro-mechanical model was programmed as a User Defined Model (UDM) in FLAC, and the explicit method is used for the finite difference calculation. The Two-Phase Flow option in FLAC is used for hydro-mechanical calculations, which involves Bishop's effective stress and the van Genuchten (1980) SWRC model. After each cycle of hydro-mechanical calculation, the SWRC corresponding to the current void ratio e is determined according to Equations (10) and (11) using FISH functions in FLAC. The degree of saturation S_r is updated according to the current suction s, both of which are used to update the mean effective stress p' for the next step of hydro-mechanical calculation.

3.2 Model calibration

Sun et al. (2007) conducted a series of tests on compacted Pearl clay involving different stress and suction paths in a triaxial cell. Results from two tests on specimens initially following a drying path (BC) and isotropic compression path under constant suction (CDE) are shown in Fig. 4. The specimen in the first test was then subjected to a wetting path under constant mean net stress (EF) after CDE as shown in Fig. 4(a), while the specimen in the second test was then subjected to a shearing path under constant suction (E'F') after CDE as shown in Fig. 4(b).

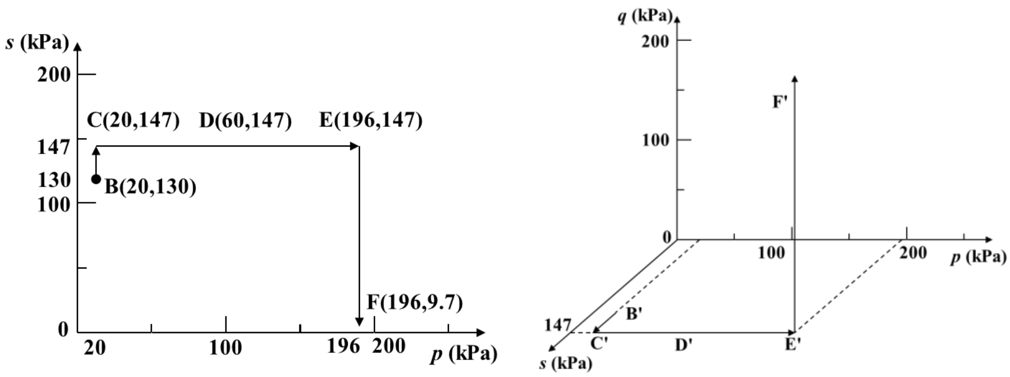

(a) (b)

Fig. 4 Stress paths and suction paths of triaxial tests: (a) with wetting path (EF) under constant mean net stress; (b) with shearing path (E'F') under constant suction (after Sun et al. 2007).

In FLAC, the triaxial tests were simulated using a single element under axisymmetric conditions with the bottom boundary fixed in the vertical direction. The pore air pressure u_a is assumed zero throughout the analysis. The wetting process is applied by the discharge function in FLAC. Specifically, during the wetting (drying) process, the water flows from the outside (inside) to the inside (outside) of the lateral boundary. Strain controlled loading is applied to the top and lateral boundaries with a low rate to ensure equilibrium for the isotropic compression stage, while stress-controlled loading is applied to the top and lateral boundaries with a small increment (decrement) for the shearing stage. The mechanical and hydraulic parameters for the compacted Pearl clay are summarized in Tables 1 and 2, respectively.

Table 1 Mechanical parameters for different soils simulated in FLAC.

Parameter	Pearl clay[a]	Minco silt[b]
Dry density, ρ_g (kg/m^3)	1500	1800
Compression index, $\lambda(0)$	0.12	0.02
Swelling index, κ	0.03	0.002
Critical state parameter, M	1.1	1.268
Atmospheric pressure, p_{at} (kPa)	101	101
Poisson's ratio, v	0.3	0.2
Parameter that controls soil stiffness with changes in suction, λ_s	0.12	0.12
Mean effective stress with no deformation when suction decreases, p'_n (MPa)	1.7	1.7

[a] after Sun et al. (2007).

[b] after Ananthanathan (2002) and Vinayagam (2004).

Table 2 Hydraulic parameters for different soils simulated in FLAC.

Parameter	Pearl clay[a]	Minco silt[b]
Fitting parameter, $1/\alpha$ (kPa)	1.322	5.813
Fitting parameter, m	0.12	0.333
Horizontal permeability coefficient, k_h (m/s)	1.0×10^{-9}	1.02×10^{-9}
Vertical permeability coefficient, k_v (m/s)	5.0×10^{-10}	1.02×10^{-10}

[a] after Sun et al. (2007).

[b] after Ananthanathan (2002) and Vinayagam (2004).

The comparison of the experimental and simulated results of the triaxial tests is shown in Fig. 5. During the drying process BC shown in Fig. 5(a), suction under constant mean net stress increases from 130 kPa to 147 kPa, and the degree of saturation decreases slightly from 52% to 51%. However, as the variation of suction is very small, the specific volume remains nearly constant. During the isotropic compression process CDE, the mean net stress increases from 20 kPa to 196 kPa under constant suction. The specific volume first decreases gradually from point C to point D where yielding occurs, and then decreases rapidly to point E. During the process of isotropic compression, the specific volume decreases, and the degree of saturation increases from 51% to 55%. This shows that the degree of saturation varies due to the change in void ratio under constant suction. Results indicate that the constitutive model can capture the influence of stress-strain behavior of unsaturated soil on the water retention behavior. During the wetting process from point E to F, the suction decreases from 147 kPa to 10 kPa under constant mean net stress, and the degree of saturation increases nonlinearly to 81%, during which a significant decrease in specific volume occurs, leading to wetting-induced deformation.

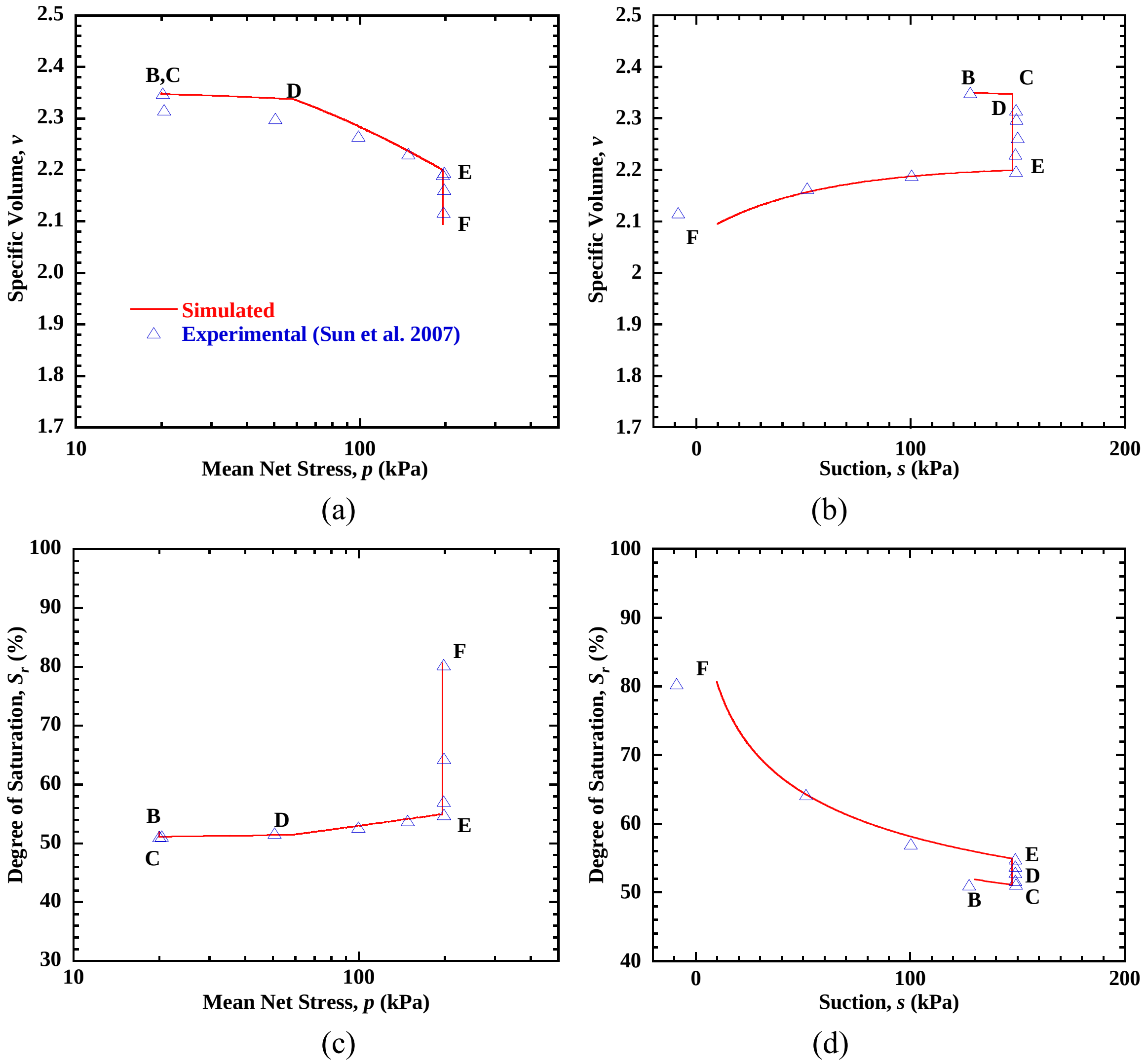

Fig. 5 Comparison between the experimental and simulated results of triaxial test under isotropic compression.

The evolution of the SWRC and LC curve during the triaxial tests is shown in Fig. 6. In

Fig. 6(a) from point B to point F, the SWRC shifts towards the right due to the decrease in void ratio. Meanwhile, as shown in Fig. 6(b), the LC yield curve expands outwards during the wetting process EF, indicating that plastic strains are generated even though the mean effective stress decreases.

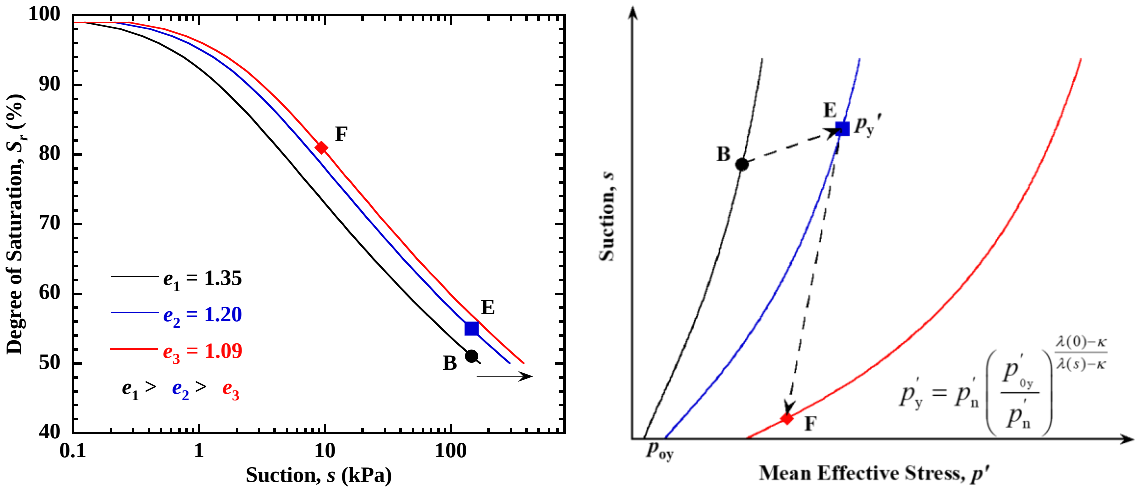

(a) (b)

Fig. 6 Evolutions of hydro-mechanical relationships: (a) SWRC; (b) LC curve.

The comparison between the experimental and simulated results of triaxial test under shearing at constant suction (s = 147 kPa) and constant mean net stress (p = 196 kPa) (i.e., stress path E'F' shown in Fig. 4b) is illustrated in Fig. 7. Results in Figs. 7(a) and 7(b) indicate that the proposed model could capture the development of shear strength and volume change during shearing under constant suction and constant mean net stress conditions. In addition, the degree of saturation gradually increases from 55% to 57% due to shear-induced volume change, as shown in Fig. 7(c), though with slight underestimation of the variation.

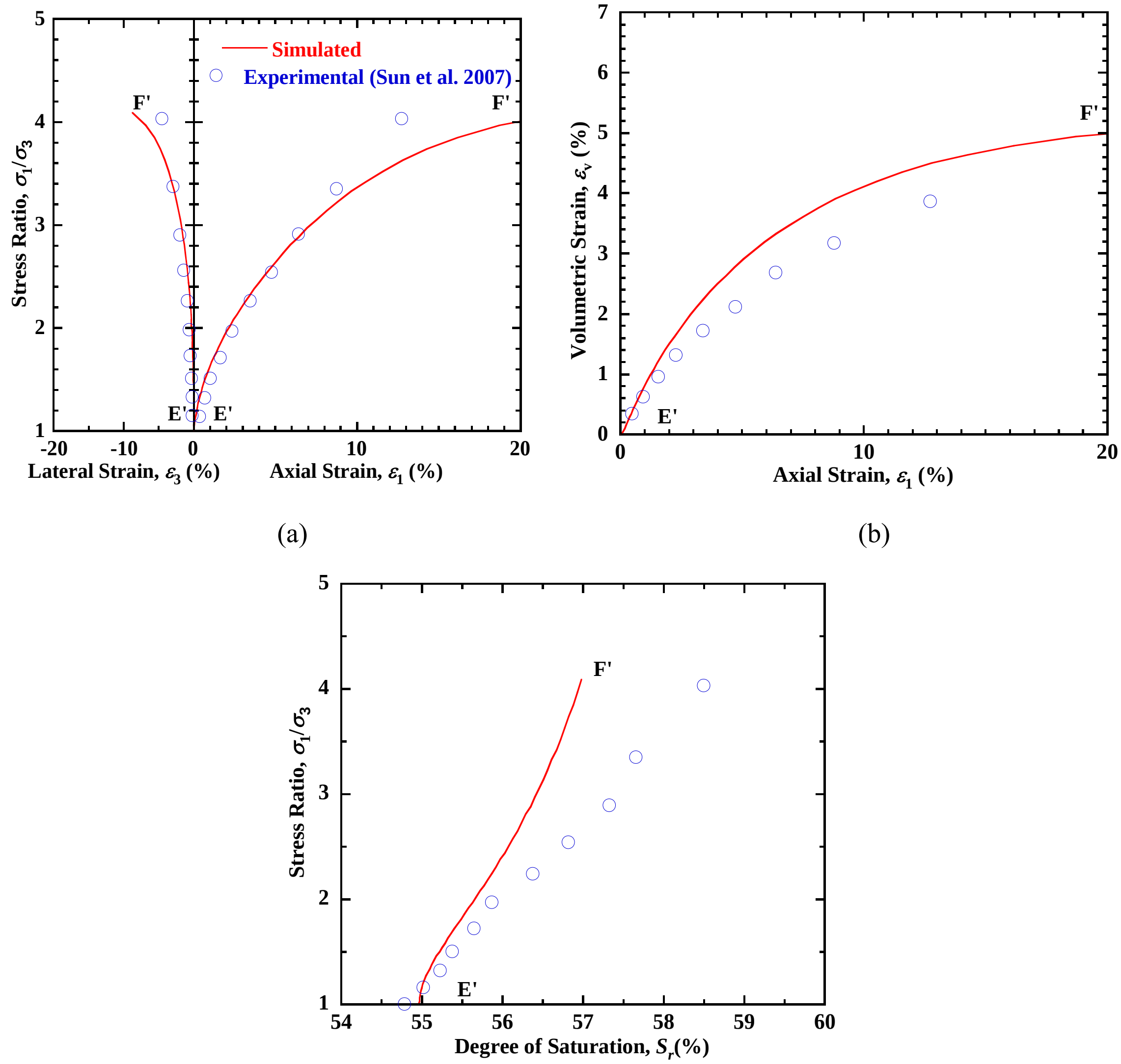

(a) (b)

(c)

Fig. 7 Comparison between the experimental and simulated results of triaxial test under shearing (s = 147 kPa and p = 196 kPa).

In general, the comparisons between experimental and simulated results in Figures 5 and 7 show that the simulated results are generally in good agreement with the triaxial test results regarding both the mechanical and hydraulic responses. The constitutive model can capture the wetting-induced deformation of unsaturated soils under constant mean net stress and the development of shear strength and volume change during shearing under constant suction and constant mean net stress. More importantly, the influence of void ratio on the water retention behavior is captured. All these confirm that the implemented constitutive model in FLAC can capture the coupled hydro-mechanical behavior of unsaturated soils during wetting.

4 Rainfall-Induced Deformations of Embankments

4.1 Model validation

The implemented constitutive model for unsaturated soils is used to simulate the wetting-induced deformations of unsaturated embankments. Miller et al. (2001) conducted three centrifuge tests of unsaturated embankment models subjected to submerging, with two embankments (Model 2 and 3) having measurements for wetting-induced settlements. The model geometry of the prototype embankment is shown in Fig. 8. The embankment had a height of 21 m and a side slope angle of $1V$:$3H$. The embankment was constructed using compacted Minco silt (Ananthanathan 2002; Vinayagam 2004). Model 2 was constructed with the fill compacted at a relative compaction (RC) of 90% and gravimetric water content of w = 10.6%, and Model 3 had RC = 95% and w = 9.6%, both of which were compacted dry of the optimum water content of 14.6%. In the numerical simulation, the compacted fill of Model 2 had initial void ratio e_0 = 0.65 and initial degree of saturation of S_{r0} = 48%, whereas e_0 = 0.60 and S_{r0} = 46% for Model 3. The model parameters for the compacted Minco silt were summarized in Tables 1 and 2. The water level was elevated from the bottom in three stages to reach nearly fully saturated conditions, as indicated in Fig. 8.

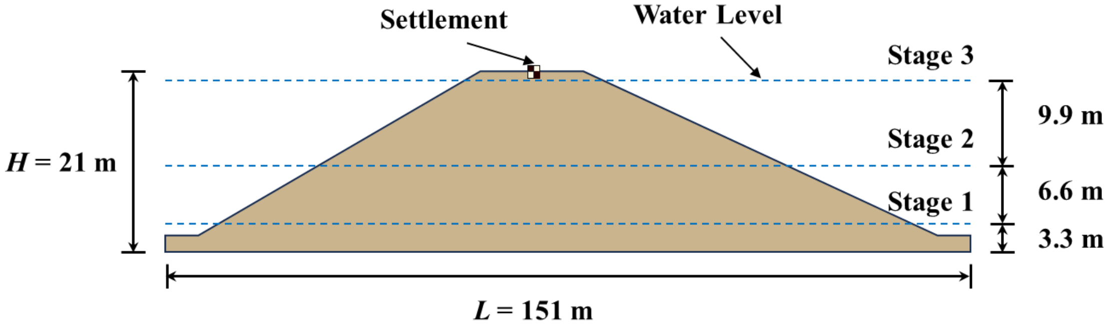

Fig. 8 Model geometry and wetting stages of prototype embankment.

The wetting-induced settlements at the top of embankment during submerging were monitored. The comparison of simulated and measured wetting-induced deformations of embankments is shown in Fig. 9. In Fig. 9(a), the results indicate that the simulated total wetting-induced settlement is in close agreement with the measured value for Model 2 but overestimates the measurement for Model 3. The incremental wetting-induced settlements of Model 3 for the three wetting stages are shown in Fig. 9(b). The simulated incremental settlements for Stage 1 and 2 are close to the measured values, while the simulated value for Stage 3 shows significant overestimation than the measurement. The simulations predicted a prototype-scale total settlement of 384 mm in the first and second stage, when the water level increased to 9.9 m, and an incremental settlement of 393 mm in the third stage, when the water level increased another 9.9 m. In the centrifuge tests, the incremental wetting-induced settlement was only 108 mm in the third stage, which is significantly lower than the total settlement of 384 mm measured in Stage 1 and 2 for the same water level rising elevation of 9.9 m. Overall, the wetting-induced deformations of embankments simulated using the proposed hydro-mechanical model for unsaturated soil could be reasonably predicted.

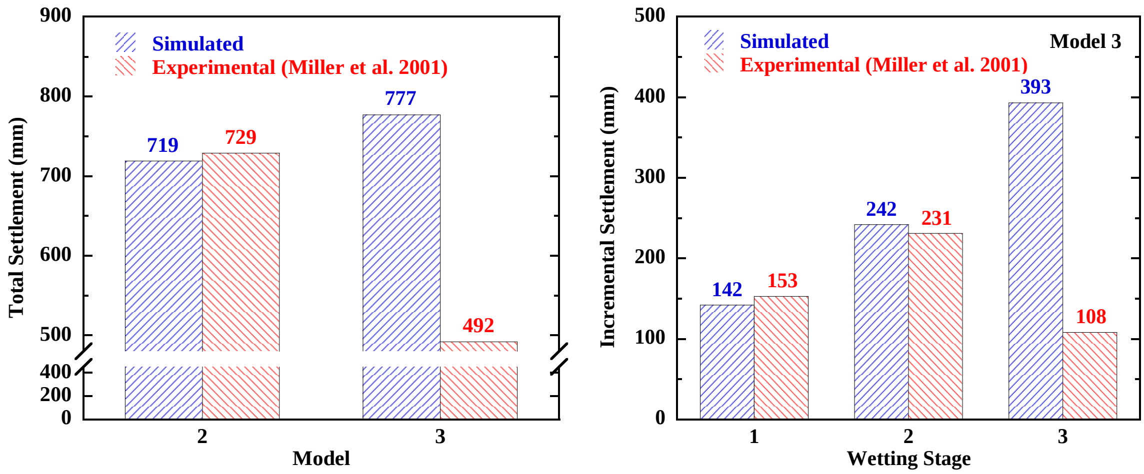

(a) (b)

Fig. 9 Comparison of simulated and measured wetting-induced deformations of embankments in prototype-scale: (a) total settlement; (b) incremental settlements.

4.2 Embankment model

The calibrated coupled hydro-mechanical constitutive model and the validated unsaturated embankment model are used to study the rainfall-induced deformation behavior of an unsaturated embankment constructed from compacted Pearl clay subjected to rainfall infiltration. Due to the symmetric nature of embankment, only half of the embankment was simulated. The geometry and boundary conditions of the embankment model are shown in Fig. 10. The embankment has a height of 6 m, a top width of 8 m, and a side slope of 1V:1.5H (vertical to horizontal). The bottom boundary of the model was fixed in the vertical and horizontal directions, and the left and right boundaries were fixed in the horizontal direction. The pore air pressure is assumed zero relative to the atmospheric pressure, which is reasonable for short embankments in the current study. The bottom and left sides of the model were set as impermeable boundaries, while the top and right sides were set as seepage boundaries. The rainfall infiltration rate was set to 20 mm/day.

For the embankment fill, the compacted Pearl clay described earlier in the calibration was simulated using the hydro-mechanical constitutive model. In the field, the embankment is compacted in layers with a specified gravimetric water content. It is typically required that the compacted embankment fill achieves a minimum relative compaction of 95%. Tatsuoka and Gomes (2018) found that the optimum degree of saturation of backfill, corresponding the optimum gravimetric water content, is around 80%, and the degree of saturation ranges from -20% to +5% of the optimum to ensure that the relative compaction is greater than 95%. Therefore, the initial degree of saturation S_{r0} of the compacted embankment fill was set to be 70% in this study, which represents a soil compacted dry of optimum and susceptible to wetting-induced deformations. The model parameters are the same as those shown in Tables 1 and 2 except the initial degree of saturation (i.e., S_{r0} = 70%). The foundation soil was simulated using the Mohr-Coulomb model with friction angle $\phi = 46^{\circ}$, Poisson's ratio $v = 0.3$, and elastic modulus E = 40 MPa. Assuming that the water table is at the surface of the foundation soil, water infiltration does not affect the behavior of foundation soil.

The foundation soil was first activated under gravitational stress conditions. The embankment fill was then constructed in layers having a thickness of 0.2 m. The embankment soil for each layer was assigned with the target compaction density and gravimetric water content (i.e., initial degree of saturation), and the mean effective yield stress corresponding to the specific elevation for each layer. For the construction of each layer, the embankment was solved for equilibrium. After construction, a steady infiltration rate was applied to the embankment top surface, slope surface, and foundation soil surface.

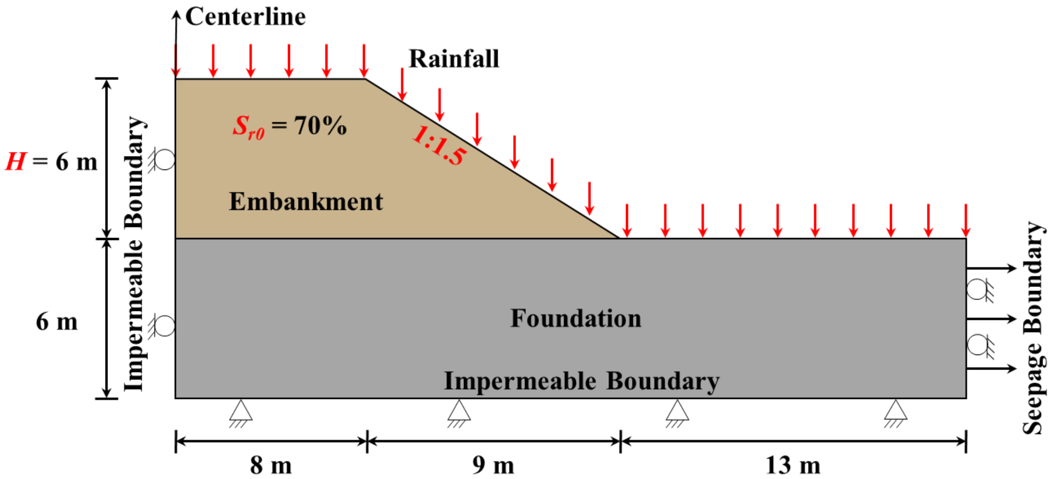

Fig. 10 Geometry and boundary conditions of embankment model.

4.3 Simulation results

The simulation results focus on the hydro-mechanical response of unsaturated embankment during the process of rainfall infiltration, including distributions of degree of saturation and suction within the embankment, settlements of the embankment surface, lateral displacements of the side slope, and volumetric strains and shear strains within the embankment. All the presented deformations are incremental with respect to those after construction.

The distributions of degree of saturation within the embankment at different cumulative infiltrations I_c during rainfall infiltration are shown in Fig. 11. The average degree of saturation S_{avg} of the entire embankment, obtained by summing up and averaging the degree of saturation of all the embankment zones, corresponding to the cumulative infiltration I_c is also indicated in the parathesis. The water infiltrated from the slope surface and the top of embankment into the embankment fill. The surface layer with a thickness of approximately 1 m, including embankment top and side slope, became saturated when the cumulative infiltration I_c reached 20 mm. After that, the wetting front moved within the embankment, and the depth of infiltration was nearly the same from both the embankment top and the side slope. The embankment became fully saturated when the cumulative infiltration reached 60 mm.

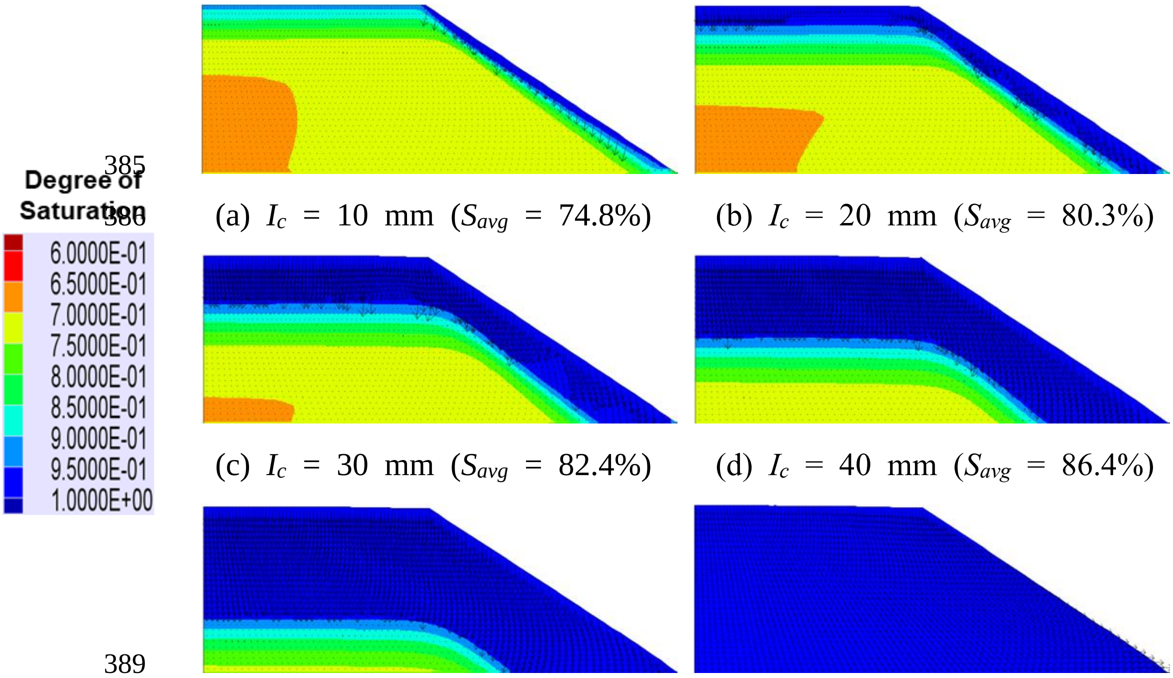

(a) I_c = 10 mm (S_{avg} = 74.8%) (b) I_c = 20 mm (S_{avg} = 80.3%)

(c) I_c = 30 mm (S_{avg} = 82.4%) (d) I_c = 40 mm (S_{avg} = 86.4%)

(e) I_c = 50 mm (S_{avg} = 96.7%) (f) I_c = 60 mm (S_{avg} = 100%)

Fig. 11 Distributions of degree of saturation at different cumulative infiltrations.

The distributions of pore water pressure within the embankment at different cumulative infiltrations I_c during rainfall infiltration are shown in Fig. 12. When the cumulative infiltration I_c reached 20 mm, positive pore water pressure appeared on the top surface and slope surface of the embankment. As the wetting front moved toward the inside of the embankment from both the top surface and slope surface, more regions have positive pore water pressure. When the cumulative infiltration reached 60 mm, the pore water pressures were positive within the entire embankment.

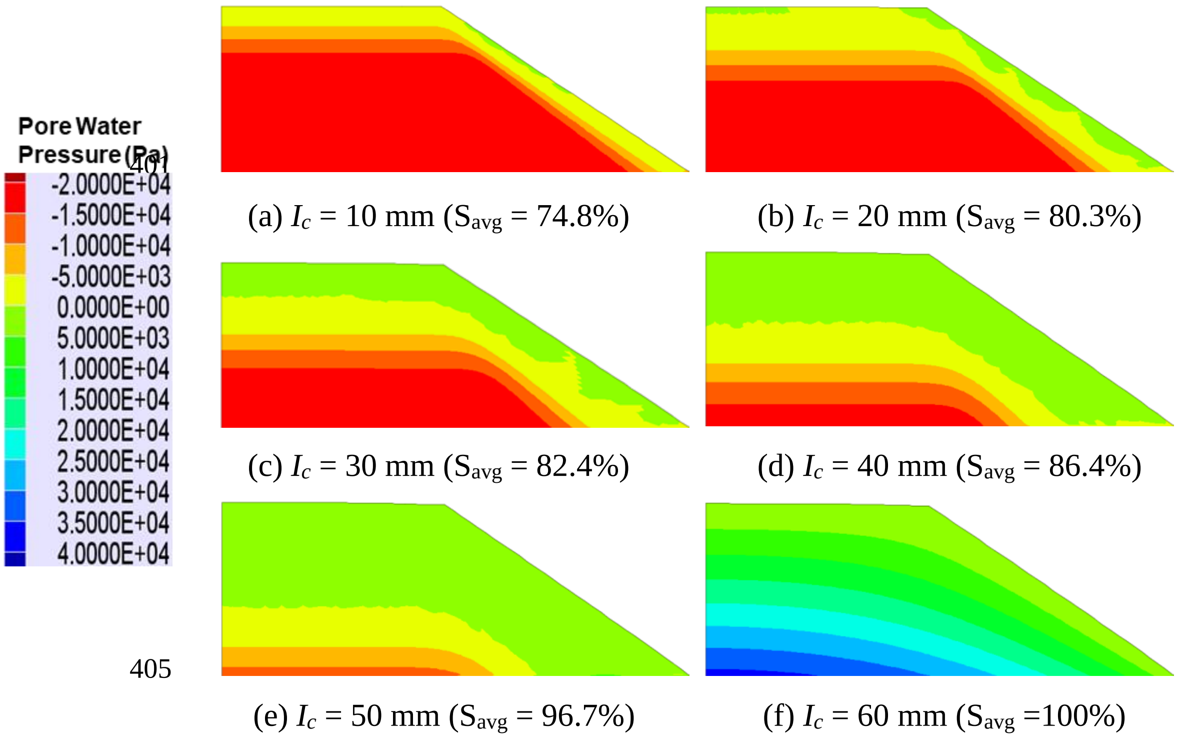

Fig. 12 Distributions of pore water pressure at different cumulative infiltrations.

Three soil elements A, B, and C along the centerline of embankment at different elevations of z = 5.0 m, 3.0 m, and 1.0 m, respectively, were monitored during rainfall infiltration. The curves of the degree of saturation S_r and suction s of embankment soil elements with the cumulative infiltration I_c are shown in Fig. 13(a). As water infiltrated into the embankment, the increase in saturation occurred simultaneously with the decrease in suction. The moment of change in degree of saturation coincided with the time of water reaching this point. The degree of saturation at soil element A started to increase when the cumulative infiltration reached 7 mm. As water infiltrated deeper into the embankment, the degrees of saturation at B and C started to increase when the cumulative infiltration reached 21 mm and 35 mm, respectively. The curves of settlement and volumetric strain of soil elements at different elevations are shown in Fig. 13(b). Taking soil element B as an example, the volumetric strain started to increase rapidly when the cumulative infiltration I_c increased to 20 mm, and reached 1.7% at I_c = 40 mm, then remained nearly constant after full saturation. The settlement at soil element B started to develop at about I_c = 30 mm, indicating that the settlement did not increase immediately when the water just infiltrated to the soil element, as the settlement was caused by the volumetric strains of deeper soil elements (e.g., C). The settlement at shallow depth (e.g., A) kept increasing until the whole embankment became fully saturated.

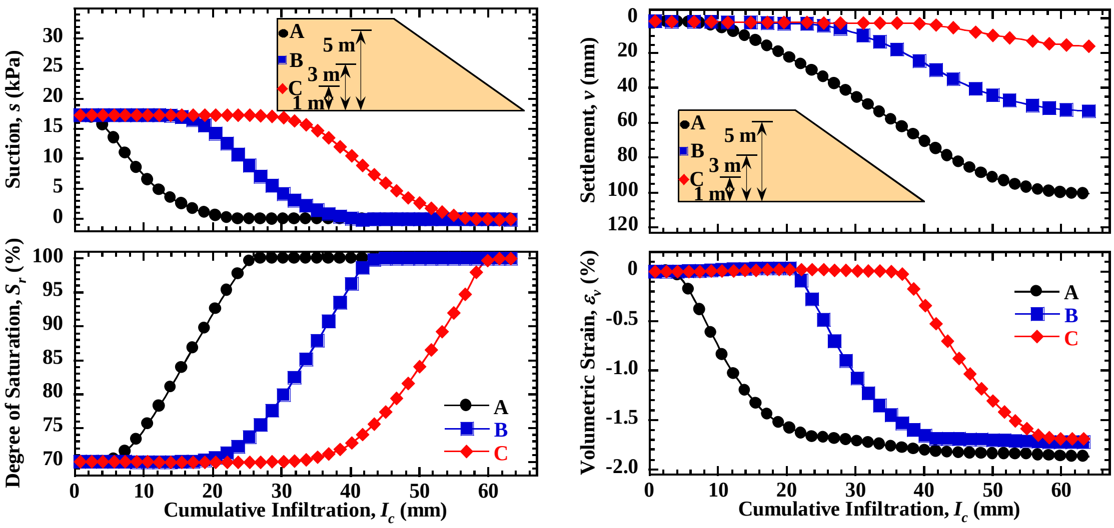

(a) (b)

Fig. 13 Hydro-mechanical response of soil elements at the centerline of embankment under transient rainfall: (a) suction and saturation; (b) settlement and volumetric strain.

Figure 14 shows the variations of mean effective stress of soil elements at the centerline of embankment under rainfall. For soil element A, as the water infiltrated, the mean effective stress decreased gradually from 20.2 kPa to 12.3 kPa, which is associated with the hydraulic component $S_r s$ in Bishop's effective stress. For deeper soil elements B and C, the effective stresses decreased slightly before the water infiltrated to the soil elements. This is attributed to the decrease in effective stresses for the shallower (upper) soil elements (e.g., A). The mean effective stresses decreased 9.1 kPa and 5.6 kPa for soil elements B and C, respectively, from initial saturation to full saturation.

The evolution of LC curves for soil elements A, B, and C along the elevation of embankment centerline from the initial state to the fully saturated state is shown in Fig. 14(b). In the initial state, the yield stress of the soil element C was higher than those of the shallower soil elements A and B due to the larger self-weight of soil. The mean effective stresses of the three soil elements with the same initial suction decreased during the rainfall, along with the decrease of corresponding yield stresses. Meanwhile, the LC curves of each soil element kept expanding, indicating yielding upon wetting and generation of plastic volumetric strains.

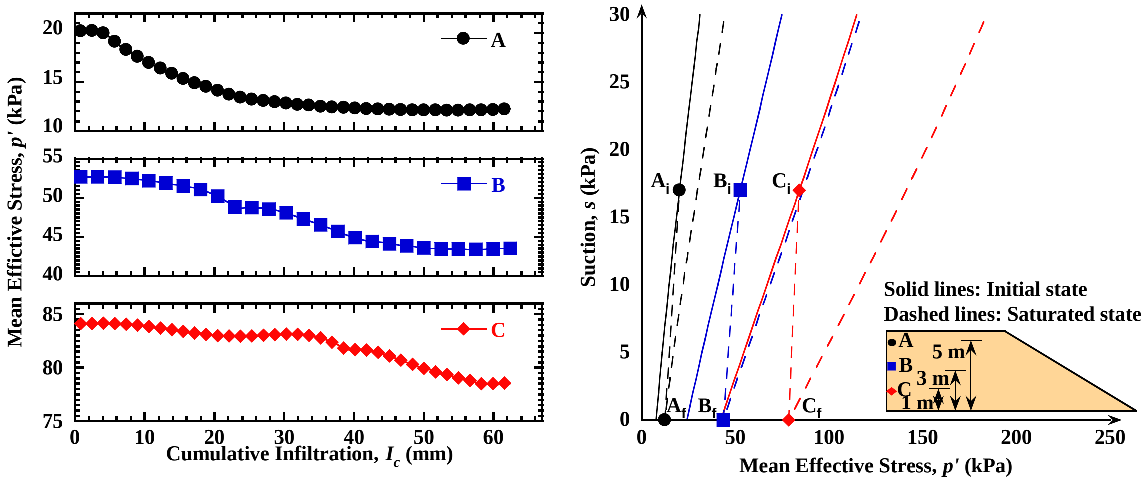

(a) (b)

Fig. 14 Evolutions of stress state of soil elements at the centerline of embankment under rainfall: (a) mean effective stresses; (b) LC curves.

The hydro-mechanical response of three soil elements D, E, and F at different elevations located 8 m away from the centerline of embankment are presented in Fig. 15. The degree of saturation and suction of soil elements near the embankment slope show the same trends as the embankment centerline, with these soil elements getting fully saturated earlier than those at the centerline, as the water infiltrated from both the top surface and the side slope of the embankment. The development of lateral displacement and shear strain of embankment soil elements with cumulative infiltration I_c is shown in Fig. 15(b). For instance, the shear strain of soil element E started to increase rapidly, when I_c increased to 18 mm, and stabilized at 2.7% for $I_c \geq 40$ mm. Soil element D near the shoulder of embankment had the maximum shear strain of 3.7%, as it is close to the potential failure surface within the embankment, while the deeper soil elements E and F had smaller shear strains. Meanwhile, the lateral displacement of soil element D showed a rapid increase from I_c = 10 mm, and then remained constant at 110 mm for $I_c \geq 40$ mm. The development of lateral displacements of embankment slope was faster than settlements along the embankment centerline due to the shorter infiltration paths.

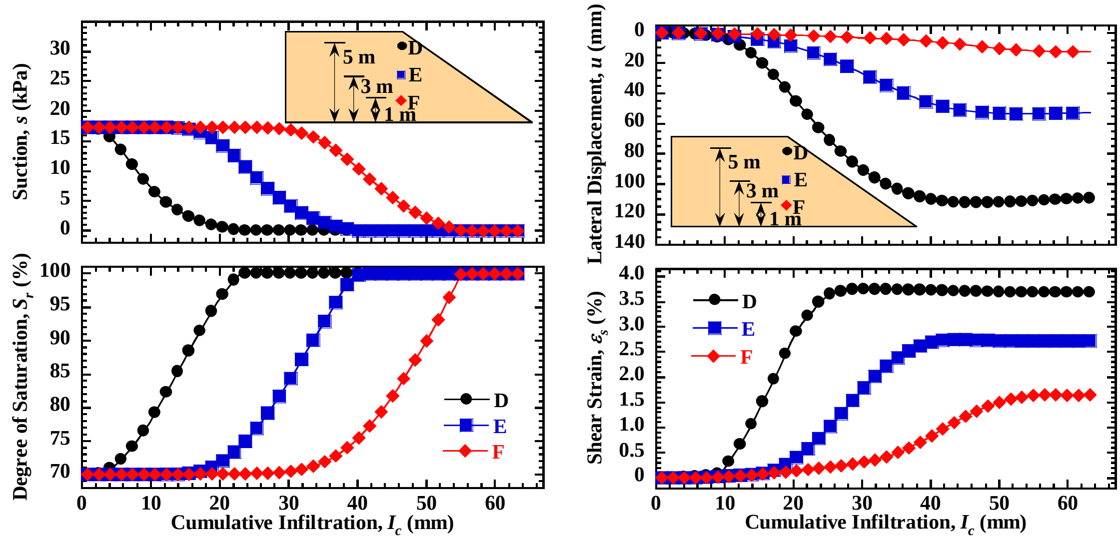

(a) (b)

Fig. 15 Hydro-mechanical response of soil elements near the slope of embankment under transient rainfall: (a) suction and saturation; (b) lateral displacement and shear strain.

The settlements of embankment top surface under rainfall are depicted in Fig. 16(a). In the initial water infiltration stage (e.g., I_c = 10 mm), the settlement of top surface was nearly uniform at 8 mm. The settlement of top surface began to increase significantly when the cumulative infiltration reached 20 mm. The settlement of top surface within 5 m from the centerline was about 22 mm. With increasing distance from the centerline, the settlement of top surface increased rapidly, reaching 48 mm at the shoulder. With further infiltration of water, settlements on the embankment top surface kept increasing significantly until the embankment reached full saturation.

The settlements of embankment centerline along the elevation under rainfall are shown in Fig. 16(b). When the cumulative infiltration is small (e.g., $I_c < 20$ mm), the settlements were negligible in the lower section of the embankment, and increased almost linearly with increasing elevation, then decreased slightly in the shallow zone of 0.2 m under the top surface of embankment. This decrease is attributed to the expansion of soil elements upon wetting for the shallow soil element under low confining stresses. The increase of settlement in the mid-height section indicates the accumulation of settlement due to wetting, and the settlement accumulation region became larger with increasing cumulative infiltration, as water infiltrated deeper into the embankment. For $I_c = 60$ mm, the settlement increased from the bottom of embankment towards the top in a linear manner, as the whole embankment became fully saturated.

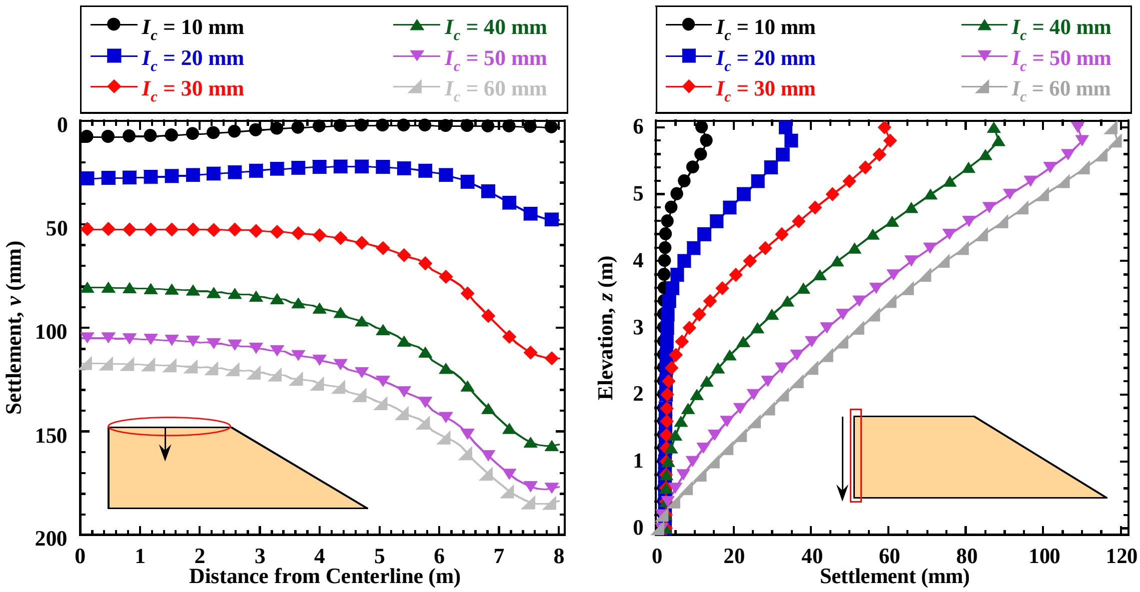

(a) (b)

Fig. 16 Settlements of embankment: (a) top surface; (b) vertical centerline.

The development of lateral displacements of embankment slope under rainfall is illustrated in Fig. 17(a). The lateral displacements of embankment slope were relatively small in the initial stage of water infiltration (e.g., I_c = 10 mm). When the cumulative infiltration I_c reached 20 mm, the lateral displacements increased significantly, and the maximum lateral displacement was 48 mm at the elevation of z = 4 m. For $I_c \geqslant$ 40 mm, the lateral displacements of embankment slope remained nearly constant with a maximum value of 143 mm. The development of the maximum lateral displacement of embankment slope under rainfall is shown in Fig. 17(b). The development process can be divided into three stages, including the slow development stage, the rapid growth stage, and the stabilization stage. The maximum lateral displacement developed at a slow rate when the cumulative infiltration was smaller than 12 mm. As the cumulative infiltration increased, the maximum lateral displacement increased significantly, and the maximum value remained constant after the cumulative infiltration reached 40 mm.

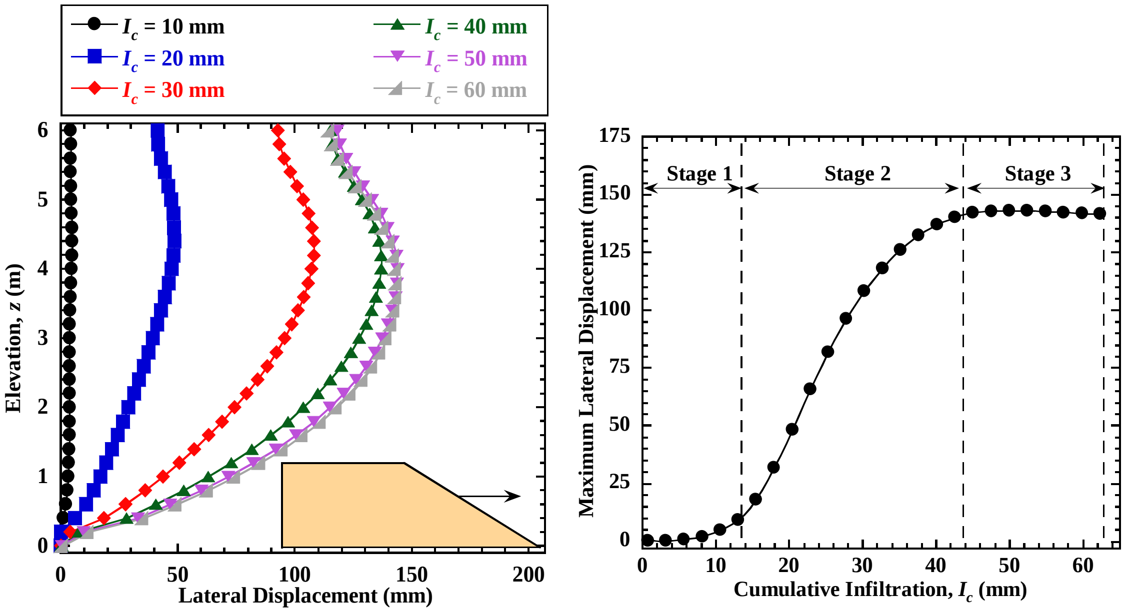

(a) (b)

Fig. 17 Lateral displacements of embankment: (a) slope surface; (b) maximum lateral displacement on slope surface.

The distributions of shear strains during rainfall infiltration are presented in Fig. 18. Shear strains were small within the embankment for I_c = 10 mm. However, for $I_c \geq$ 20 mm, shear strains started to develop in a shallow region along the slope surface. As the cumulative infiltration increased, the shear strains kept accumulating and increased towards the toe of slope, forming of a prominent plastic shear zone. After the embankment was fully saturated, the embankment slope remained stable. However, the shear strain contours indicate the formation of a potential failure surface at a shallow depth of approximately 2 m from the slope surface.

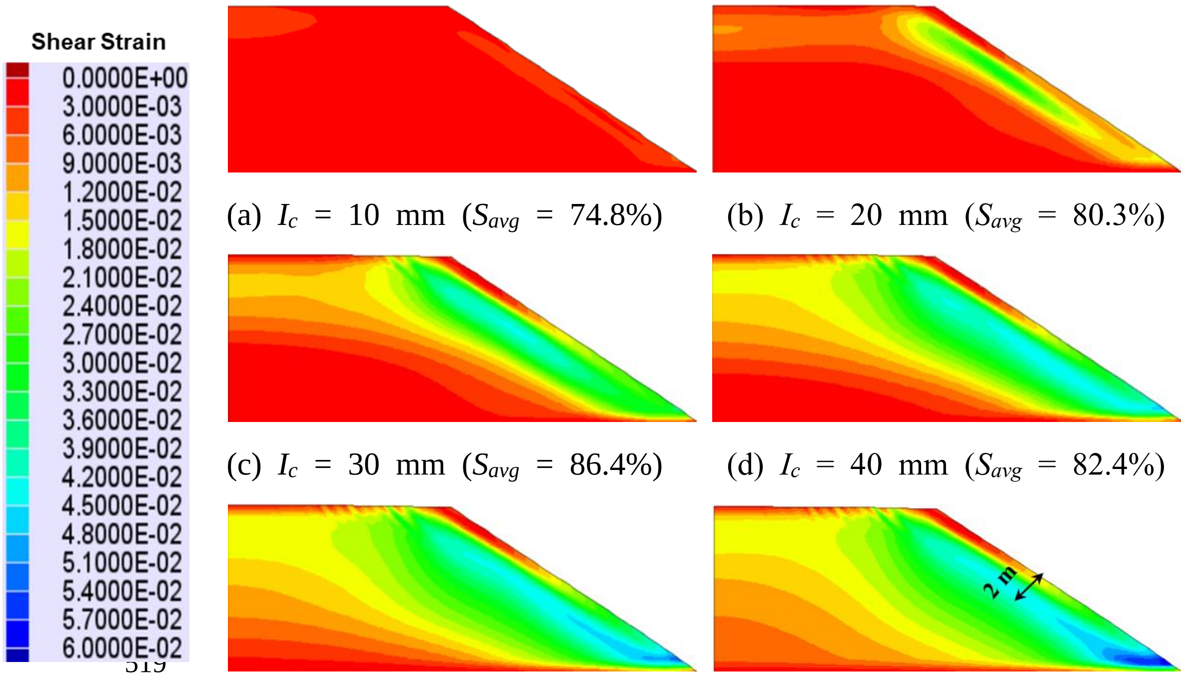

(a) I_c = 10 mm (S_{avg} = 74.8%) (b) I_c = 20 mm (S_{avg} = 80.3%)

(c) I_c = 30 mm (S_{avg} = 86.4%) (d) I_c = 40 mm (S_{avg} = 82.4%)

(e) I_c = 50 mm (S_{avg} = 96.7%) (f) I_c = 60 mm (S_{avg} = 100%)

Fig. 18 Distributions of shear strain for different cumulative infiltrations.

5 Parametric study

A parametric study is conducted to investigate the influences of slope angle and embankment height on the rainfall-induced deformations of unsaturated embankments. Simulation results focus on the settlements of embankment top surface and lateral displacements of embankment slope surface. All the presented deformations are incremental with respect to those after construction.

5.1 Influence of slope angle

Embankments with the same height of 6 m and different slope angles of 1*V*:1*H*, 1*V*:1.25*H*, 1*V*:1.5*H*, 1*V*:1.75*H*, and 1*V*:2*H* were investigated. All embankments had an initial degree of saturation of S_{r0} = 70% and were brought to full saturation under rainfall. The settlements of embankment top surface for different slope angles due to rainfall are shown in Fig. 19(a). The results show that after full saturation, the variations in settlement are not significant near the centerline of the embankments with different slope angles, but the settlements near the shoulder increase as the slope angle increases. The settlement at the shoulder increases from 150 mm to 185 mm when the slope angle increases from 1V:2H to 1V:1.5H. A sharp increase of settlements is observed 6 m away from the centerline when the slope angle further increases to 1V:1H, and the settlement at the shoulder reaches approximately 320 mm. This can be attributed to the larger shear stresses developed within the steep slopes, which result in significant downward movements upon wetting. Results indicates that settlements near the embankment shoulder increase significantly for slope angle beyond 1V:1.5H, resulting in large differential settlement on the embankment surface, which would affect the service performance of embankments. As shown in Fig. 19(b), the settlements of the centerline for the embankment with different slope angles are similar, indicating that the slope angle has little influence on the settlements of embankment centerline, as the centerline is far from the slope surface.

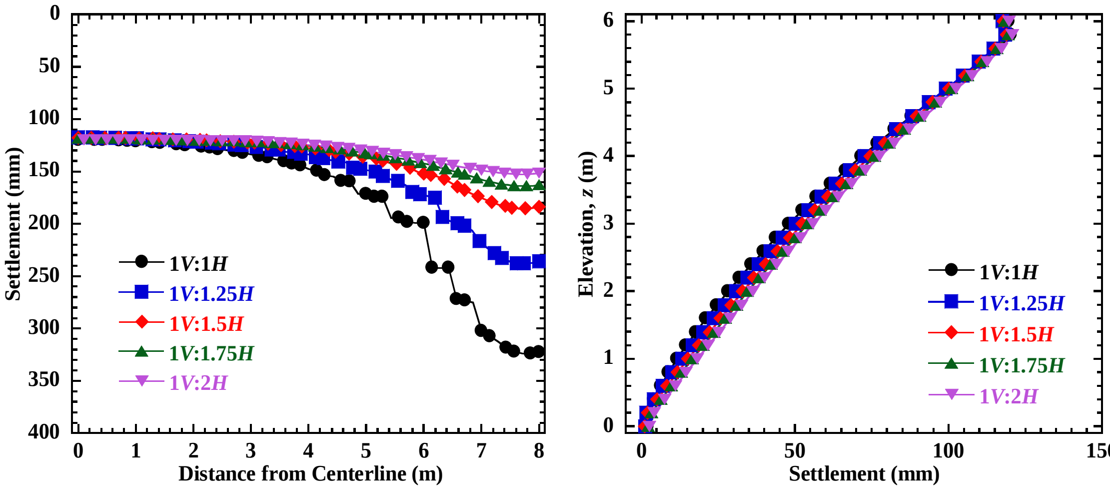

(a) (b)

Fig. 19 Influence of embankment slope angle on settlements: (a) top surface; (b) vertical centerline.

Fig. 20(a) displays lateral displacements of the embankments with different slope angles after full saturation. Lateral displacement profiles of slope surface all show a consistent trend with the maximum displacement at the elevation of z = 4 m. Similar to the embankment settlements, lateral displacements increase rapidly for slope angle greater than 1V:1.5H. Fig. 20(b) shows that the maximum lateral displacement increases from 95 mm to 143 mm, as the slope angle increases from 1V:2H to 1V:1.5H, and the maximum displacement progressively increases to 291 mm at 1V:1H.

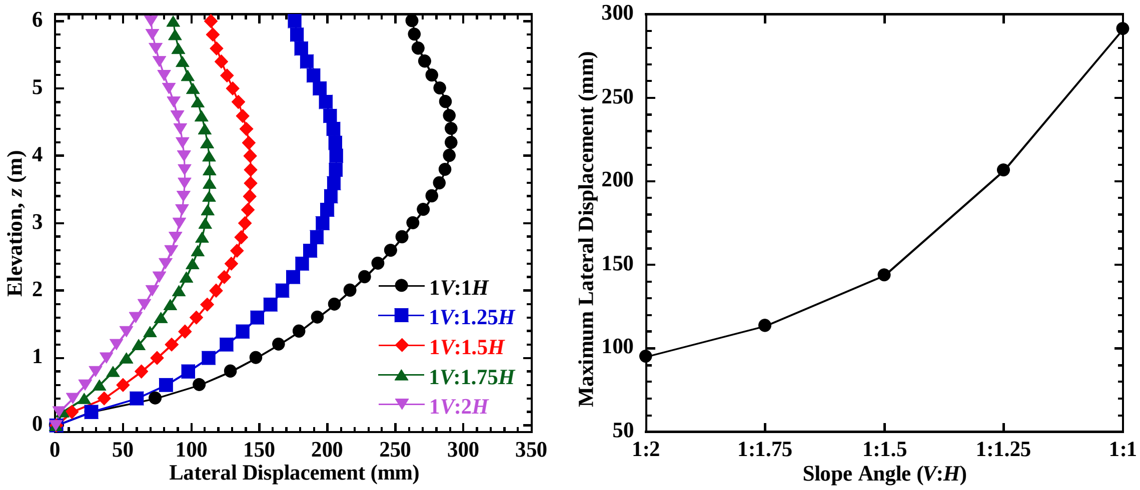

(a) (b)

Fig. 20 Influence of embankment slope angle on lateral displacements: (a) slope surface; (b) maximum lateral displacement.

5.2 Influence of embankment height

The embankments with different heights of 4 m, 6 m, 8 m, and 10 m were considered to investigate the influence of embankment height on the rainfall-induced deformations. All embankments had a slope angle of 1V:1.5H and an initial degree of saturation of S_{r0} = 70%. In Fig. 21(a), the settlements of embankment top surface increase with the height of embankment, which is attributed to the higher confining stress conditions associated with taller embankments and the larger volume of backfill for compression. In addition, the differential settlement between the embankment centerline and shoulder increases significantly from 39 mm for H = 4 m to 105 mm for H = 10 m due to the large settlements developed at the shoulder upon wetting. The settlements of embankment centerline versus normalized elevation after full saturation are shown in Fig. 21(b). A small amount of expansion is observed near the top surface for all four cases. However, the accumulation rates of settlement along the centerline are different, with the settlements developing much faster for taller embankments due to the higher confining stress conditions.

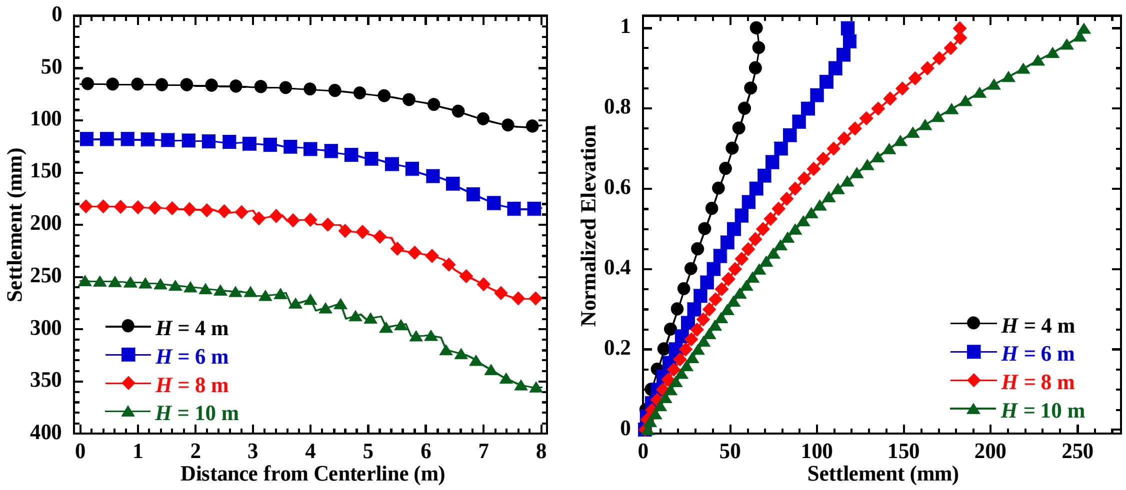

(a) (b)

Fig. 21 Influence of embankment height on settlements: (a) top surface; (b) vertical centerline.

The lateral displacements of embankment slope after full saturation for different embankment heights are shown in Fig. 22. The lateral displacements of slope also increase with increasing embankment height, and the maximum value increases linearly from 78 mm for H = 4 m to 282 mm for H = 10 m. For different embankment heights, the maximum lateral displacements all occurred at the elevations ranging from 0.6H to 0.7H.

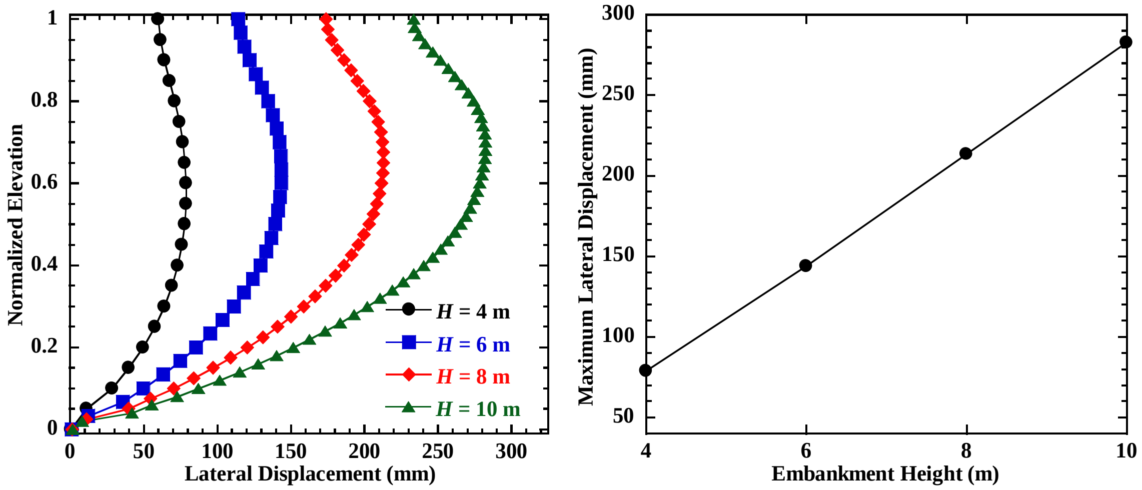

(a) (b)

Fig. 22 Influence of embankment height on lateral displacements: (a) slope surface; (b) maximum lateral displacement.

6 Conclusions

A coupled hydro-mechanical constitutive model for unsaturated soils was introduced and implemented in the finite difference program FLAC. The model was successfully calibrated using triaxial test data on unsaturated soils and validated using measurements of wetting-induced deformations of embankments tested in a geotechnical centrifuge. These demonstrate that the constitutive model of unsaturated soils can capture the coupled hydro-mechanical behavior of unsaturated soils for wetting conditions and could be used to investigate boundary value problems. The model was then applied to investigate the hydro-mechanical response of unsaturated embankments subjected to rainfall infiltration to understand the influences of embankment slope angle and height on the rainfall-induced deformations of embankments. The following conclusions are reached for the conditions investigated in this study:

(1) As water infiltrates into the embankment, the degree of saturation increases and suction

in the soil elements change as expected. As the wetting front moves toward the inside of the embankment, more regions have positive pore water pressures. The variations of degree of saturation and suction lead to a decrease in the effective stress and yield stress in the soil. The expansion of the LC curves during this process indicates yielding upon wetting and generation of plastic, contractive volumetric strains.

(2) During rainfall infiltration, the differential settlement on the top surface between the centerline and shoulder increase significantly, which could result in severe damage to the overlying structures. Along the elevation of embankment centerline, the shallow zone of 0.2 m experiences slight expansion upon wetting under low confining stress, while the settlements underneath the shallow zone accumulate as the rainfall infiltrates deeper into the embankment, and the settlement accumulation region becomes larger with increasing cumulative infiltration.

(3) As the cumulative infiltration increases, the shear strains keep accumulating and increase towards the toe of slope, forming of a prominent plastic shear zone. After the embankment was fully saturated, the maximum lateral displacement increased significantly, but the embankment slope remained stable. However, the shear strain contours indicate the formation of a potential failure surface at a shallow depth of approximately 2 m from the slope surface, even though failure may not occur.

(4) The geometry of embankments plays a significant role in the rainfall-induced deformations of embankments. The differential settlements on the embankment top surface and the maximum lateral displacements of embankment slope surface increase significantly with increasing slope angle. For slope angle greater than $1V$:$1.5H$, more attentions should be paid on the design embankment shoulder due to wetting. The wetting-induced deformations also

increase with increase embankment height, and the maximum lateral displacements all occur at the elevations of 0.6H to 0.7H.

Declaration of competing interest

The authors declare that they have no known competing financial interests or personal relationships that could have appeared to influence the work reported in this paper.

Acknowledgments

This research work is supported by the National Natural Science Foundation of China (Grant No. 52078392), the National Key R&D Program of China (Grant No. 2022YFC3080400), and the Fundamental Research Funds for the Central Universities (Grant No. 2042023kfyq03 and 2042023kf1014). The authors appreciate the financial supports.

References

Abbate, A., Papini, M., Longoni, L., 2021. Analysis of meteorological parameters triggering rainfall-induced landslide: a review of 70 years in Valtellina. Natural Hazards and Earth System Sciences, 21, 2041–2058.

Adams, B., 1996. Critical state behaviour of an agricultural soil. Ph.D. thesis. The University of Saskatchewan, Canada.

Alonso, E., Gens, A., Josa, A., 1990. A constitutive model for partially saturated soils. Geotechnique, 40, 405–430.

Alonso, E., Olivella, S., Pinyol, N., 2005. A review of Beliche Dam. Géotechnique, 55, 267–

285.

Ananthanathan P. 2002. Laboratory Testing of Unsaturated Minco Silt, MS Thesis, University of Oklahoma, Norman.

Chiu, C., Ng, C., 2003. A state-dependent elasto-plastic model for saturated and unsaturated soils. Geotechnique, 53, 809–829.

Cui, Y.J., Delage, P., 1996. Yielding and plastic behaviour of an unsaturated compacted silt. Géotechnique 46, 291–311.

Gallipoli, D., Gens, A., Sharma, R., Vaunat, J., 2003. An elasto-plastic model for unsaturated soil incorporating the effects of suction and degree of saturation on mechanical behaviour. Geotechnique, 53, 123–135.

Gallipoli, D., Wheeler, S.J., Karstunen, M., 2003. Modelling the variation of degree of saturation in a deformable unsaturated soil. Geotechnique, 53, 105–112.

Gens, A., 1996. Constitutive modelling: application to compacted soils. In: Alonso EE, Delage P, editors. Unsaturated soils, vol. 3. Rotterdam: Balkema; 1996. p. 1179–200.

Gens, A., 2009. Some issues in constitutive modelling of unsaturated soils. Presented at the 4th Asia-Pacific Conference on Unsaturated Soils, Taylor and Francis, pp. 613–626.

Georgiadis, K., Potts, D.M., Zdravkovic, L., 2005. Three-Dimensional Constitutive Model for Partially and Fully Saturated Soils. International Journal of Geomechanics 5, 244–255.

Jamei, M., Guiras, H., Olivella, S., 2015. Analysis of slope movement initiation induced by rainfall using the Elastoplastic Barcelona Basic Model. European Journal of Environmental and Civil Engineering, 19, 1033–1058.

Jotisankasa, A., Ridley, A., Coop, M., 2007. Collapse behavior of compacted silty clay in suction-monitored oedometer apparatus. Journal of Geotechnical and Geoenvironmental Engineering, 133, 867–877.

Kato, S., Karube, D., Honda, M., Fujiwara, T., 1996. Influence of water distribution on the compression behavior of unsaturated soil. JSCE, 554/III-37, 57–69 (in Japanese).

Karube, D., Honda, M., Kato, S. and Tsurugasaki, K., 1997. The relationship between shearing characteristics and the composition of pore-water in unsaturated soil. JSCE, 575/III-40, 49–58 (in Japanese).

Khalili, N., Habte, M.A., Zargarbashi, S., 2008. A fully coupled flow deformation model for cyclic analysis of unsaturated soils including hydraulic and mechanical hystereses. Computers and Geotechnics, Special Issue on Unsaturated Soils: Models, Algorithms and Applications. Computer and Geotechnics, 35, 872–889.

Khosravi, A., McCartney, J.S., 2012. Impact of Hydraulic Hysteresis on the Small-Strain Shear Modulus of Low Plasticity Soils. Journal of Geotechnical and Geoenvironmental Engineering 138, 1326–1333.

Lee, I., Sung, S., Cho, G., 2005. Effect of stress state on the unsaturated shear strength of a weathered granite. Canadian Geotechnical Journal, 42, 624–631.

Lim, T., Rahardjo, H., Chang, F., Fredlund, G., 1996. Effect of rainfall on matric suctions in a residual soil slope. Canadian Geotechnical Journal, 33, 618–628.

Lu, N., J. W. Godt, and D. T. Wu. 2010. A closed-form equation for effective stress in unsaturated soil. Water Resources Research, 46 (5): W05515.

McCartney, J.S., Behbehani, F., 2021. Hydromechanical behavior of unsaturated soils: Interpretation of compression curves in terms of effective stress. Soil. Rocks 44, e2021065721.

Miller, G.A., Khoury, C.N., Muraleetharan, K.K., Liu, C., Kibbey, T.C.G., 2008. Effects of soil skeleton deformations on hysteretic soil water characteristic curves: Experiments and simulations. Water Resources Research, 44, 5.

Miller, G.A., Muraleetharan, K.K., and Lim, Y.Y. 2001. "Wetting-induced settlement of compacted fill embankments." Transportation Research Record, 1755, 111–118.

Mitchell, J. K., Hooper, D. R., and Campanella, R. G. 1965. "Permeability of compacted clay." J. Soil Mech. Found. Div., 91(SM4), 41–65.

Moriwaki, H., Inokuchi, T., Hattanji, T., Sassa, K., Ochiai, H., Wang, G., 2004. Failure processes in a full-scale landslide experiment using a rainfall simulator. Landslides, 1, 277–288.

Mun, W., McCartney, J.S., 2017. Constitutive Model for Drained Compression of Unsaturated Clay to High Stresses. Journal of Geotechnical and Geoenvironmental Engineering 143, 04017014.

Nuth, M., Laloui, L., 2008. Advances in modelling hysteretic water retention curve in deformable soils. Computer and Geotechnics, 35, 835–844.

Olivella, S., Gens, A., Carrera, J., Alonso, E.E., 1996. Numerical formulation for a simulator (CODE_BRIGHT) for the coupled analysis of saline media. Engineering Computations, 13, 87–112.

Rutqvist, J., Ijiri, Y., Yamamoto, H., 2011. Implementation of the Barcelona Basic Model into TOUGH–FLAC for simulations of the geomechanical behavior of unsaturated soils. Computers and Geosciences 37, 751–762.

Sassa, K., Tsuchiya, S., Ugai, K., Wakai, A., Uchimura, T., 2009. Landslides: a review of achievements in the first 5 years (2004–2009). Landslides, 6, 275–286.

Sharma, R., 1998. Mechanical behaviour of unsaturated highly expansive clays. Ph.D. thesis, University of Oxford, Oxford, UK.

Sheng, D., Fredlund, D.G., Gens, A., 2008. A new modelling approach for unsaturated soils using independent stress variables. Canadian Geotechnical Journal, 45, 511–534.

Sivakumar, V., Wheeler, S.J., 2000. Influence of compaction procedure on the mechanical behaviour of an unsaturated compacted clay. Part 1: Wetting and isotropic compression. Géotechnique, 50, 359–368.

Sun, D., Matsuoka, H., Yao, Y., Ichihara, W., 2000. An Elasto-Plastic Model for Unsaturated Soil in Three-Dimensional Stresses. Soils and Foundations, 40, 17–28.

Sun, D., Sheng, D., Sloan, S., 2007. Elastoplastic modelling of hydraulic and stress–strain behaviour of unsaturated soils. Mechanics of Materials, 39, 212–221.

Sun, D., Sun, W., Xiang, L., 2010. Effect of degree of saturation on mechanical behaviour of unsaturated soils and its elastoplastic simulation. Computers and Geotechnics, 37, 678–688.

Sun, D., Sheng, D.C., Cui, H., Sloan, S., 2007. A density-dependent elastoplastic hydro-mechanical model for unsaturated compacted soils. International Journal for Numerical and Analytical Methods in Geomechanics, 31, 1257–1279.

Sun, W., Sun, D., 2012. Coupled modelling of hydro-mechanical behaviour of unsaturated compacted expansive soils. International Journal for Numerical and Analytical Methods in Geomechanics 36, 1002–1022.

Thu, T., Rahardjo, H., Leong, E., 2007. Critical State Behavior of a Compacted Silt Specimen. Soils and Foundations, 47, 749–755.

Toll, D.G., 1990. A framework for unsaturated soil behaviour. Géotechnique, 40, 31–44.

Tatsuoka, F., Gomes Correia, A., 2018. Importance of controlling the degree of saturation in soil compaction linked to soil structure design. Transportation Geotechnics, 17, 3–23.

Van Genuchten, M.Th., 1980. A Closed-form Equation for Predicting the Hydraulic Conductivity of Unsaturated Soils. Soil Science Society of America Journal 44, 892–898.

Vanapalli, S.K., Fredlund, D.G., Pufahl, D.E., 1999. The influence of soil structure and stress history on the soil–water characteristics of a compacted till. Géotechnique, 49, 143–159.

Vinayagam T. 2004. Understanding the Stress–Strain Behavior of Unsaturated Minco Silt using Laboratory Testing and Constitutive Modeling, MS Thesis, University of Oklahoma, Norman.

Wang, L., Zhang, G., Zhang, J.-M., 2010. Nail Reinforcement Mechanism of Cohesive Soil Slopes Under Earthquake Conditions. Soils and Foundations, 50, 459–469.

Wang, S., Idinger, G., Wu, W., 2021. Centrifuge modelling of rainfall-induced slope failure in variably saturated soil. Acta Geotechnica, 16, 2899–2916.

Wheeler, S.J., 1996. Inclusion of specific water volume within an elasto-plastic model for unsaturated soil. Canadian Geotechnical Journal, 33, 42–57.

Wheeler, S.J., Sharma, R.S., 1995. An elasto-plastic critical state framework for unsaturated soil. Geotechnique, 45(1), 35–53.

Wheeler, S.J., Sharma, R.S., Buisson, M.S.R., 2003. Coupling of hydraulic hysteresis and stress–strain behaviour in unsaturated soils. Geotechnique, 53(1), 41–54.

Wheeler, S.J., Sivakumar, V., 2000. Influence of compaction procedure on the mechanical behaviour of an unsaturated compacted clay. Part 2: shearing and constitutive modelling. Géotechnique, 50, 369–376.

Xiong, Y., Ye, G., Xie, Y., Ye, B., Zhang, S., Zhang, F., 2019. A unified constitutive model for unsaturated soil under monotonic and cyclic loading. Acta Geotechnica, 14, 313–328.

Zakaria, I., 1994. Yielding of unsaturated soil. Ph.D. thesis, University of Sheffield, UK.

Zhang, F., Ikariya, T., 2011. A New Model for Unsaturated Soil Using Skeleton Stress and Degree of Saturation as State Variables. Soils and Foundations, 51, 67–81.

Zhang, G., Qian, J., Wang, R., Zhang, J., 2011. Centrifuge Model Test Study of Rainfall-Induced Deformation of Cohesive Soil Slopes. Soils and Foundations 51, 297–305.

Zheng, Y., Hatami, K., Miller, G.A., 2017. Numerical Simulation of Wetting-Induced Settlement of Embankments. Journal of Performance of Constructed Facilities, 31, D4017001.

Zhou, A., Sheng, D., 2015. An advanced hydro-mechanical constitutive model for unsaturated soils with different initial densities. Computers and Geotechnics, 63, 46–66.

Zhou, A., Sheng, D., Sloan, S., Gens, A., 2012a. Interpretation of unsaturated soil behaviour in the stress – Saturation space, I: Volume change and water retention behaviour. Computers and Geotechnics, 43, 178–187.

Zhou, A., Sheng, D., Sloan, S., Gens, A., 2012b. Interpretation of unsaturated soil behaviour in the stress–saturation space: II: Constitutive relationships and validations. Computers and Geotechnics 43, 111–123.